Science Advances
AAAS

advances.sciencemag.org/cgi/content/full/5/10/eaav3140/DC1

Supplementary Materials for

Electrically control amplified spontaneous emission in colloidal quantum dots

Junhong Yu, Sushant Shendre, Weon-kyu Koh, Baiquan Liu, Mingjie Li, Songyan Hou, Chathuranga Hettiarachchi,
Savas Delikanli, Pedro Hernández-Martínez, Muhammad Danang Birowosuto, Hong Wang, TzeChien Sum,
Hilmi Volkan Demir*, Cuong Dang*

*Corresponding author. Email: volkan@stanfordalumni.org (H.V.D.); hcdang@ntu.edu.sg (C.D.)

Published 25 October 2019, *Sci. Adv.* **5**, eaav3140 (2019)
DOI: 10.1126/sciadv.aav3140

This PDF file includes:

Fig. S19. Population dynamics under an electric field of ~21 kV/cm and with a pump fluence of 100 μJ/cm^2.
Fig. S20. Population dynamics under an electric field of ~21 kV/cm and with a pump fluence of 1000 μJ/cm^2.
References (*39–45*)

Section S1. Electric field and current in the CQD device

a. Determine the electric field applied on CQDs

Here, the two electrodes and the wire we used have negligible resistance compared to that of the layered device. Our capacitor device with 3 dielectric layers is equivalent to 3 capacitors in series. Using a reference capacitor[11], we can calculate the voltage cross the CQD layer (fig. S1):

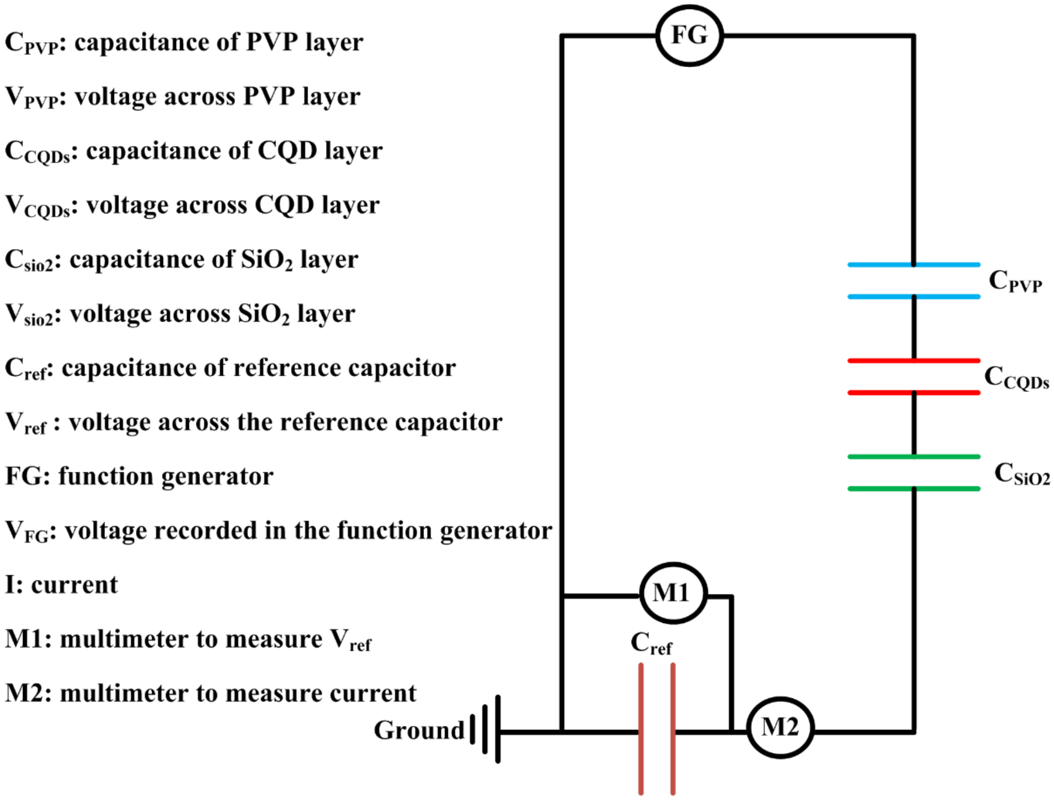

C_{PVP}: capacitance of PVP layer

V_{PVP}: voltage across PVP layer

C_{CQDs}: capacitance of CQD layer

V_{CQDs}: voltage across CQD layer

C_{sio2}: capacitance of SiO_2 layer

V_{sio2}: voltage across SiO_2 layer

C_{ref}: capacitance of reference capacitor

V_{ref} : voltage across the reference capacitor

FG: function generator

V_{FG}: voltage recorded in the function generator

I: current

M1: multimeter to measure V_{ref}

M2: multimeter to measure current

Fig. S1. Schematics of the circuit. Function generator model: FG500A, WAVETEK.

Here, we have a circuit with four capacitors in series

$$V_{FG}=V_{ref}+V_{SiO_2}+V_{CQD}+V_{PVP}$$

$$Q_{ref}=Q_{SiO_2}=Q_{CQD}=Q_{PVP}=V_{ref}\times C_{ref}$$

Then, we can derive that

$$V_{SiO_2}=\frac{V_{ref}\times C_{ref}}{C_{SiO_2}};V_{PVP}=\frac{V_{ref}\times C_{ref}}{C_{PVP}}$$

Just plug into the voltage formula

$$V_{CQD} = V_{FG} - V_{ref} - \frac{V_{ref} \times C_{ref}}{C_{SiO_2}} - \frac{V_{ref} \times C_{ref}}{C_{PVP}}$$

Now we only need the capacitance of SiO_2 and PVP layer to calculate the voltage drop across the CQD layer. As described in method, we can calculate the capacitance using the following

$$C = \frac{A \times \varepsilon_0 \times \varepsilon_r}{d}$$

Where A is the area of the capacitor (8 mm * 2 mm), d is the thickness of each layer determined by the SEM measurement (also supported by the surface profiler measurement, fig. S2) and ε_0 is the permittivity of vacuum and ε_r is the relative permittivity of each dielectric film.

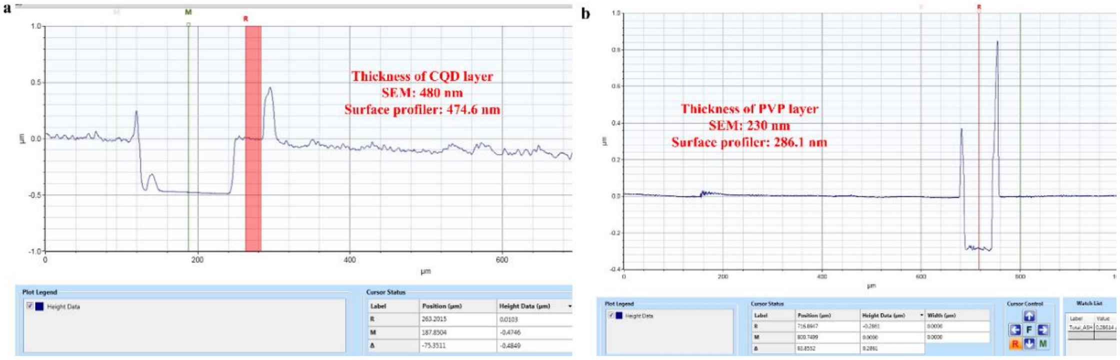

Label	Position (µm)	Height Data (µm)
R	263.2015	0.0103
M	187.8504	-0.4746
Δ	-75.3511	-0.4849

Label	Position (µm)	Height Data (µm)	Width (µm)
R	716.8947	-0.2861	0.0000
M	800.7499	0.0000	0.0000
Δ	83.8552	0.2861	

Label	Value
Total_ASH	0.28614

Fig. S2. Thickness measurement conducted by surface profiler (DektakXT surface profiler). (**a**) CQD layer. It shows good consistence with the SEM result (**b**) PVP layer. The slight difference between SEM result and surface profiler measurement is caused by spin-casting films on different substrates: the PVP layer is on top of CQD layer in SEM measurement, while in surface profiler measurement, the PVP layer is spin-casted on a glass substrate.

Relative permittivity is measured using an ellipsometer (VASE, J.A. Woollam, spectral range from 193 nm to 3200 nm) and the results are shown in fig. S3:

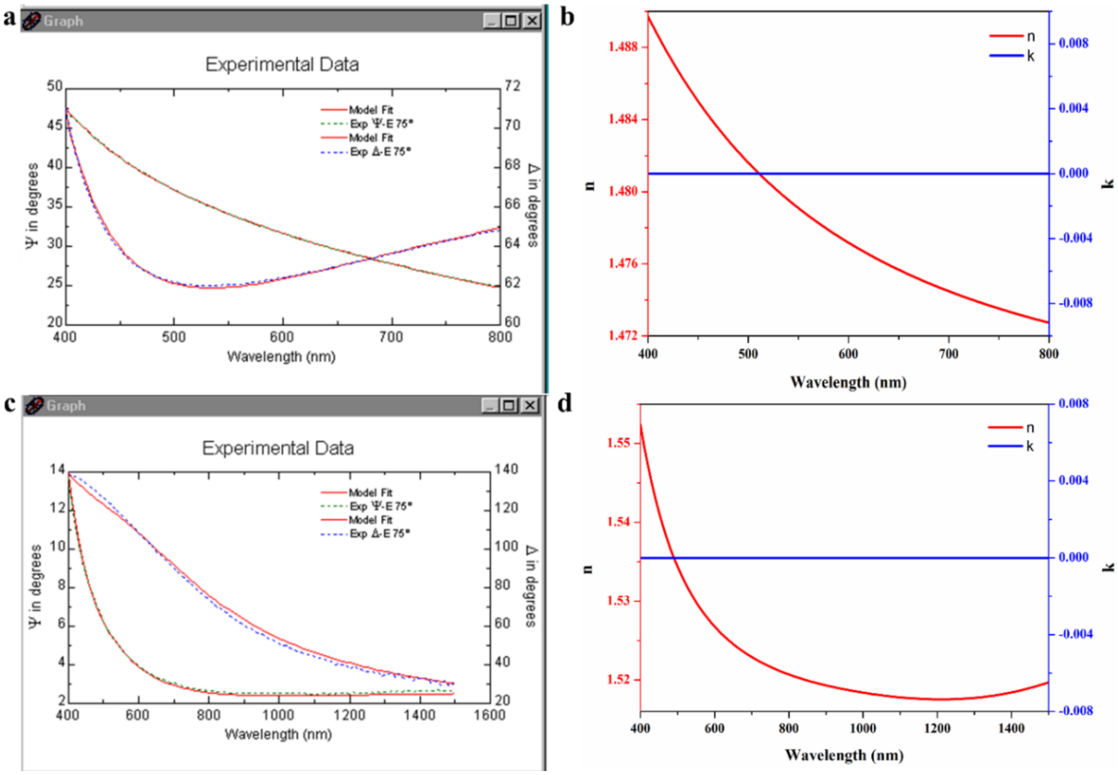

Fig. S3. Permittivity measurement result. (**a**) Fitting result of SiO_2 film. (**b**) n and k of SiO_2 film. (**c**) Fitting result of PVP film. (**d**) n and k of PVP film.

We can see that the refractive index does not change too much in the visible wavelength range. Here we adopt the average refractive index (SiO_2: 1.48, PVP: 1.53) at the visible spectrum to approximate the materials' permittivity at very low frequency. Finally, we can calculate the electric field applied on the CQD film in the device from the voltage and the thickness of this layer.

Considering we utilized the average refractive index to evaluate the capacitance of the insulator layers, combining with the measurement error, it is essential to calibrate the voltage drop across the CQD layer. Here, we have fabricated the capacitor without CQD layer (the SEM picture of the structure is shown in fig. S4a, the thickness of these two insulator layers are the same compared to the device used in the Fig. 1c). Firstly, we will use the calculated capacitance of SiO_2 layer to extract the voltage drop across the PVP layer. Then, we will use the calculated capacitance of PVP layer to extract the voltage drop across the SiO_2 layer. Since the equality of the charge of each capacitor is always true in a serial capacitor circuit, if the charge stored in SiO_2 layer (Q = C*V, C is calculated via the thickness and permittivity of SiO_2, V is extracted using the capacitance of PVP) is equal to (in an acceptable way) the charged is stored in PVP layer (Q = C*V, C is calculated via the thickness and permittivity of PVP, V is extracted using the capacitance of SiO_2), then we can conclude that our method should be reliable. The result is shown in fig. S4b, we can see that the deviation between the charges stored in these two layers is acceptable.

$$V_{applied} = V_{ref} + V_{SiO_2} + V_{PVP}$$

$$V_{SiO_2} = V_{applied} - V_{ref} - V_{ref} \times \frac{C_{ref}}{C_{PVP}}$$

$$V_{PVP} = V_{applied} - V_{ref} - V_{ref} \times \frac{C_{ref}}{C_{SiO_2}}$$

$$V_{PVP} \times C_{PVP} \overset{?}{=} V_{SiO_2} \times C_{SiO_2}$$

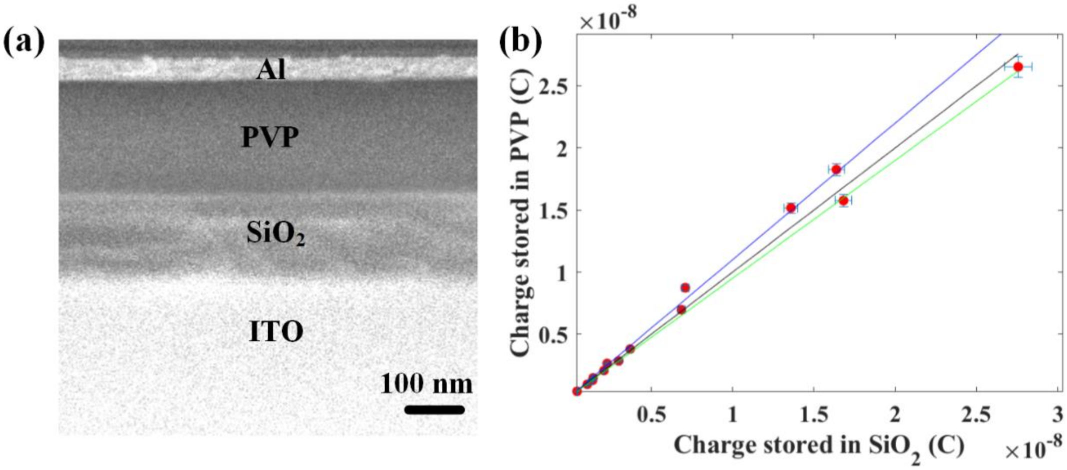

Fig. S4. Mutual corroboration to calibrate the voltage drop. (**a**) The SEM image of the device without CQD layer. (**b**) The Charge stored in SiO_2 and PVP layer. The slope of the black line is 1. The slope of the blue line is 1.1. The slope of the green line is 0.95.

b. The mechanism of electron injection

The energy level schematic of the device is shown in fig. S5. As it can be seen, compared to the LED device, the electrons and holes can’t be directly injected into the QDs due to the two high energy barriers (SiO_2 and PVP layer). The main reason for us to choose the capacitor structure is that these two insulator layers can avoid CQDs being directly adjacent to electrodes (causing emission quench) and limits the electrical current to allow us to charge the CQDs controllably. Worth to mention that, we did not choose the CQDs sandwiched by two SiO_2 layers, as did in ref. 11, because the sputtering process can greatly degrade the optical gain performance of CQDs. For spontaneous emission, the emission degradation is less important, thus this will not be an issue for the authors of ref. 11. Here, we spin-casted the PVP polymer as another insulator layer.

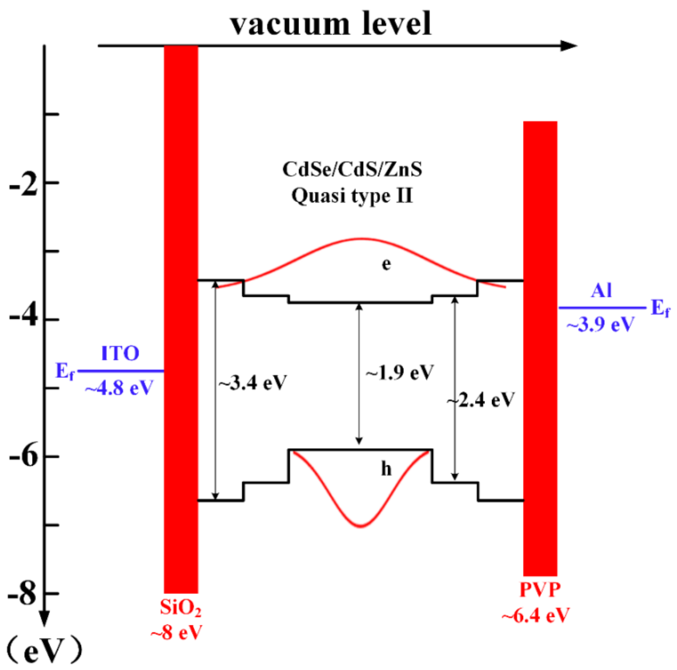

Fig. S5. Energy schematic of the device. The energy level values for CdSe/CdS/ZnS QDs are obtained from ref. 27. The energy level values for ITO and Al are taken from ref. 39. The energy level value for SiO_2 is taken from ref. 11. The energy level value for PVP is obtained from ref. 40.

In the device (a Sawyer−Tower circuit), capacitors in series share the charge that moved between them[11]. When electric field was applied, the electrons/holes were accumulated at the interface of insulator/CQDs. There's a probability for them to tunnel into the CQDs. However, in quasi-type II CQDs, the energy barrier for electrons and holes are quite different (the hole wave function is well-confined in the core, while the electron wave function is delocalized over the whole core/shell/shell structure). Meanwhile, the effective mass of electron ($m_e^* = 0.13m_0$) in CdSe is much smaller than the effective mass of hole ($m_h^* = 0.3m_0$)[42]. We can use the following equation[41] to roughly estimate the tunneling efficiency of electrons and holes

$$T = \{1 + \frac{(\mathrm{e}^{\kappa L} - \mathrm{e}^{-\kappa L})^2}{16\frac{E}{V}(1-\frac{E}{V})}\}^{-1}$$

$$\kappa = \sqrt{\frac{2m^*}{\hbar^2}(\mathrm{V}-\mathrm{E})}$$

Where E is electron or hole energy, V is the height of the energy barrier, L is the width of the barrier. For electrons, the wave function is spreading through the core and shells so the barrier width is very small (smaller than ZnS shell thickness of ~ 1.3 nm due to the delocalization). While the hole wave function is confined in the core only, the barrier width is much thicker (~ CdS/ZnS shell/shell thickness of ~ 2.5nm). Thus, the possibility for hole tunneling is negligible compared to that for electrons.

c. The current flow through the device

The current flowing through the circuit was recorded by the multimeter as a function of V_{FG} (fig. S6). The current is stable in the order of 100 nanoampere for entire range of electric field, indicating good insulating layers between two electrodes. The effect of applied electric field on CQDs is dominant in our device.

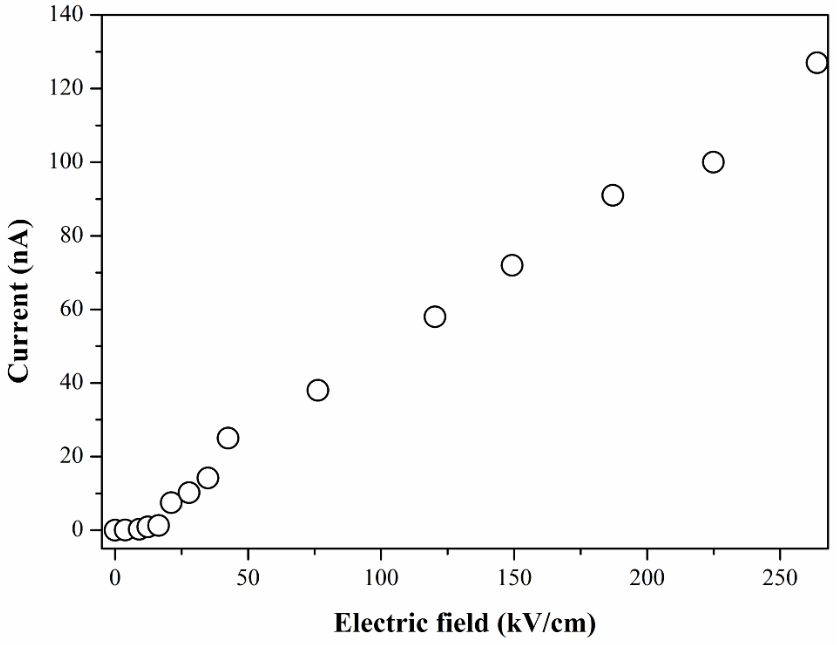

Fig. S6. Measured current flowing through the circuit.

It is worth to note that fig. S6 shows the stable AC current while the DC current behaved very unstable. The DC current started in the nanoampere range as AC current then increased gradually to few tens of microampere in the time frame of seconds to minutes. The slow behavior of DC current suggests chemical changes in CQD film during the DC current. The process can be repeated again if the device is rested after a run. This indicated the reversible process was happening in the CQD film under DC bias. The AC bias (few hundred Hz) was chosen to achieve very stable current and consistent optical properties of CQD film.

Section S2. ASE in the CQD device without electric field

The amplified spontaneous emission (ASE) behavior of CQD layer in the device under 500 ps laser pulse excitation (532 nm) is shown in fig. S7. The emission spectra were measured at different pump fluences (from 270 μJ/cm^2 to 1605 μJ/cm^2). In the device, with the two dielectric layers as spacers from two electrodes, our CQD film's emission was not quenched and its optical gain is excellent. If pump fluences are beyond threshold, we can see a shoulder appearing at ~640 nm, which indicates the start of ASE. As presented in fig. S7b and fig. S7c, the large reduction in the FWHM and sudden increase in the peak intensity of the edge emission also provide a strong evidence of transition from spontaneous emission to ASE. The signature of biexciton gain is observed with red-shift of ASE peak from spontaneous emission peak (fig. S7e). The threshold extracted from the log-log fitting of the light input-light output curve is ~891 μJ/cm^2, which is higher than the value in previous reports[27] (threshold of CdSe/CdS/ZnS CQDs is ~600 μJ/cm^2, corresponding <N> is ~1.9, pump by femtosecond pulse laser, 480 nm).

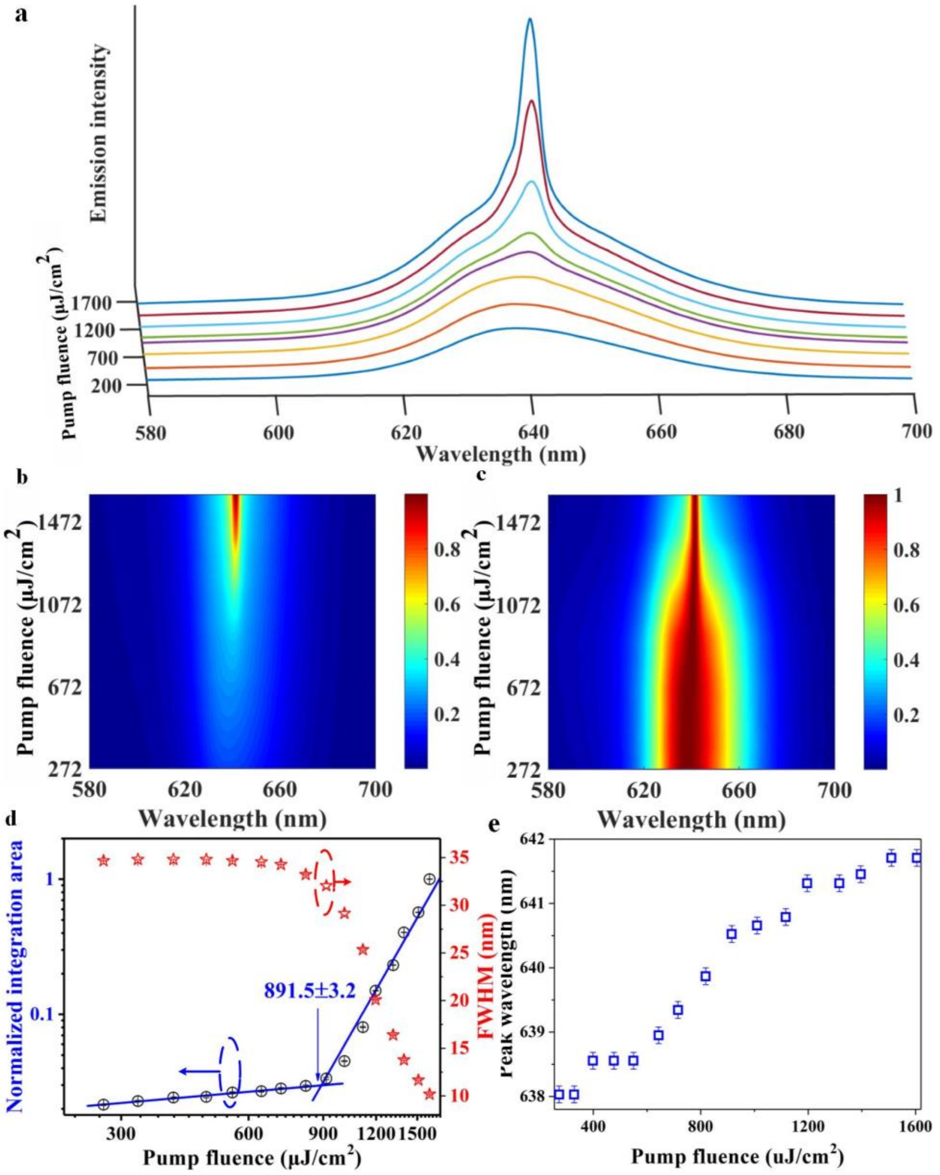

Fig. S7. Edge emission as a function of pump fluence without electric field under 500-ps laser pulse excitation (532 nm). (**a**) Emission spectra. (**b**) The 2d spectra map normalized by the peak ASE intensity at the maximum pump fluence to show the intensity increase of ASE peak. (**c**) The 2d spectra map normalized by the peak intensity at each pump fluence to show the narrowing effect of ASE peak. (**d**) Integrated emission intensity (log-log plotting) and the FWHM of emission profile (semi-log plotting) as a function of pump fluence. (**e**) The peak wavelength of ASE as a function of pump fluence.

As mentioned in the main text, three effects here are responsible for the increased ASE threshold. (1) The multiple layers can cause the pump fluence reduction because the reflection and scattering are each layer and their interfaces. (2) Compared with femtosecond laser, our 0.5 ns pulsed laser pump has to compete with very fast non-radiative Auger recombination to build up the population inversion and results in higher threshold. (3) The reduction of CQD absorption cross-section at our pumping wavelength (532 nm) when compared to that at femtosecond pump wavelength (480 nm). To make the threshold comparison valid, we also pumped our CQDs with 100 fs laser pulse excitation (400 nm), the extracted threshold is ~53 μJ/cm^2, corresponding <N> is 1.29, suggesting the good performance of our CQDs in terms of optical gain.

Section S3. Steady-state absorption measurement

a. Measurement set-up

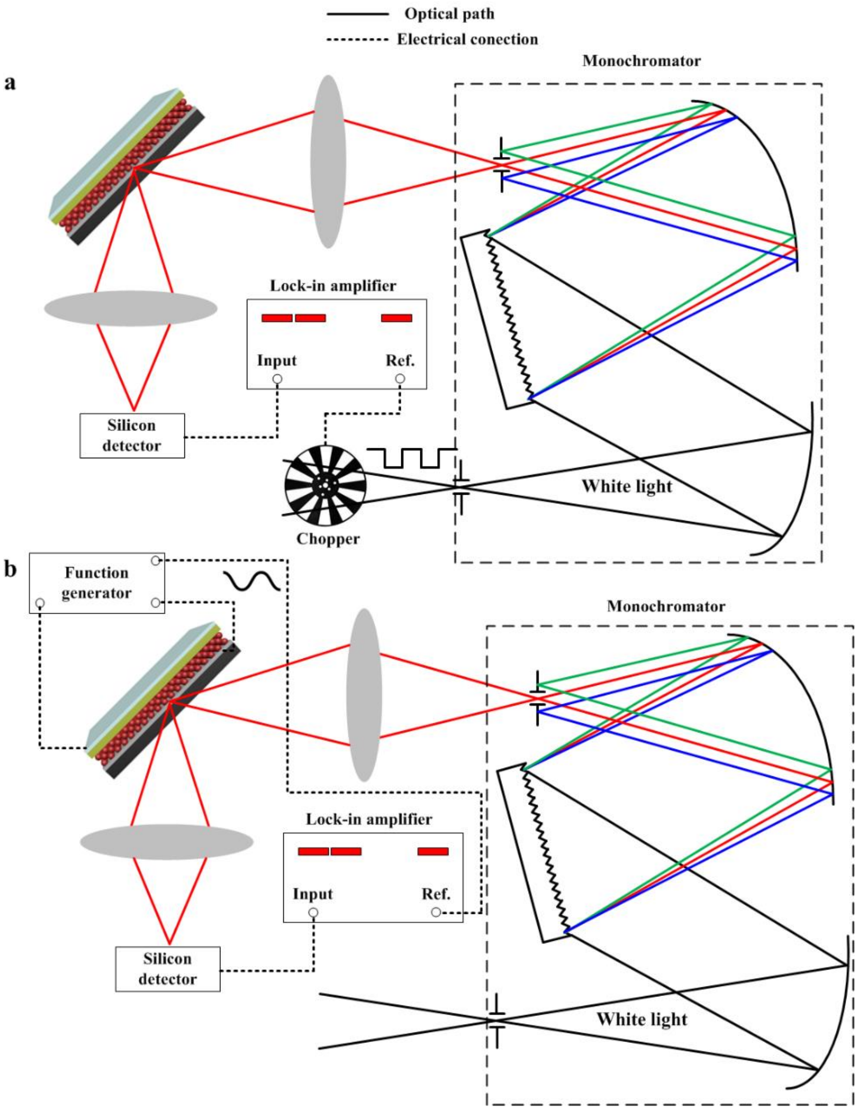

Fig. S8. Measurement setup for electric field–dependent absorbance. (**a**) The set-up for measurement of steady state absorbance. The chopper synced signal was used as the lock-in reference. (**b**) The set-up for measurement of absorption modulation under AC electric filed. The synced signal from function generator was used as the lock-in reference.

The measurement setup is shown in fig. S8. The white light generated by the light source (ELS-250, Asahi Spectra) was filtered by a monochromator (7ISWS, spectral selection range: 330~1000 nm) and then focused onto the device from the ITO glass substrate at the angle of 45 °. A silicon photodetector (Newport 2031, 400~1070 nm) was used to collect the reflection light off the device. The signal from the silicon photodetector was analyzed by a lock-in amplifier (SR830, Stanford Research System). To calculate the electric field-modulated absorbance of the CQD layer only, we need to measure both the absolute reflection of the device (without electric field) and the modulated reflection when applying electric field. Here, we used an optical chopper (MC1000, THORLABS) to modulate the illumination light when no electric field was applied. By chopping the light, we can measure light intensity precisely with lock-in technique, therefore reflectivity can be calculated correctly as many commercial instruments do. After that, the lock-in technique (locked to bias modulation frequency) does not measure the reflection anymore, it measures the amplitude of reflectivity change directly when electric field is applied.

b. Optical bleaching calculation

The first step is to figure out the absorbance (or transmittance) of CQD film in the device structure without electric field. As we mention in the device fabrication process (methods), we had two different sets of samples (device) on the same substrate. One was with the CQD layer, another one was without the CQD layer. Basically, we used an optical chopper to modulate the illumination light and measured the lock-in voltage for two different structures without electric field (fig. S8a).

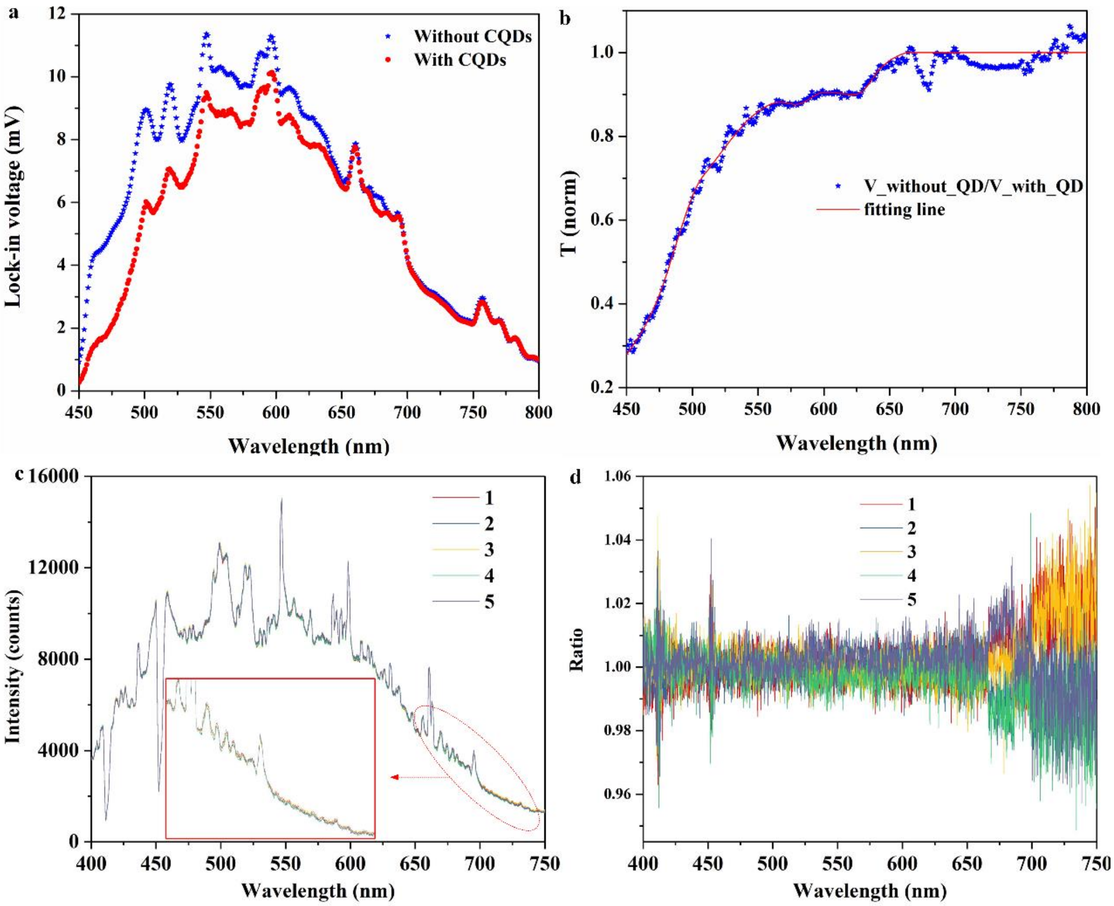

Fig. S9. Measuring the transmittance of the CQD layer. (**a**) Lock-in voltages with the light modulated by the optical chopper. (**b**) The calculated transmittance (blue dots) and fitting result (red solid line). (**c**) The spectrum of light source. The inset is the zoom-in of low energy tail. **(d)** The intensity fluctuation which is divided by the averaged value.

Then we can calculate the absorbance of CQD layer using the following

$$V_{without\_CQDs}^{chop} = K_1 \times I(\lambda) \times R(\lambda)_{without\_CQDs}^{0}$$
$$V_{with\_CQDs}^{chop} = K_2 \times I(\lambda) \times R(\lambda)_{with\_CQDs}^{0}$$

Where, I(λ) is the wavelength dependent light intensity of the white light source. K_1 and K_2 is the experimental coefficient which takes care all the correction for experimental setup and equipment response such as the optical alignment or detector gain setting. $R(\lambda)^0$ is the reflectance for each case.

Considering the only difference between two cases is the CQD layer, then we can have this relationship

$$R(\lambda)^0_{with\_\mathrm{C}QDs} = T(\lambda)^0_{CQDs} \times R(\lambda)^0_{without\_\mathrm{C}QDs}$$

Where, $T(\lambda)^0_{CQD}$ is the transmittance of CQD layer without electric field. The light is passing through the CQD layer twice when it reflects off the Al electrode. Here, in the reflection measurement, $T(\lambda)^0_{CQD}$ represents the equivalent transmittance of the CQD layer in the reflection measurement. Then, we can have this relationship via combining these two equations

$$\mathrm{T}(\lambda)^0_{CQDs} = \frac{R(\lambda)^0_{with\_\mathrm{C}QDs}}{R(\lambda)^0_{without\_\mathrm{C}QDs}} = \frac{K_2}{K_1} \times \frac{V^{chop}_{with\_\mathrm{C}QDs}}{V^{chop}_{without\_\mathrm{C}QDs}}$$

Now our task becomes finding out the value of K_2/K_1. It is always true that our CQD layer does not absorb light beyond 660 nm, so we just need to find the ratio that makes the two lock-in voltage overlapping to the maximum extent beyond 660 nm. Here the ratio in our case is 1.437, as shown in fig. S8a. Then, we conduct the fitting (fig. S9b) and convert transmittance to absorbance.

We notice that, in fig. S9b, variations in the 670-700 nm range is large. We measure the spectra of the light source for 5 times shown in fig. S9c), as it can be seen, there are two low intensity spikes (around 420 nm and 452 nm) and one low intensity tail (beyond 660 nm). When the light intensity is low, the signal to noise ratio (SNR) is low as we can see the larger measured intensity fluctuation at long wavelength (> 5%, as shown in fig. S9d). This variation will have a negligible effect on our interpretation. The reasons are as following: (1) When the wavelength is longer than 660 nm, the absorbance of CdSe/CdS/ZnS QDs is infinitely close to zero; (2) For the interested wavelength range (460~650 nm), the intensity variation is acceptable (< 2%), and we can well-fit the transmission by choosing a proper ratio and the two absorption feature ($1S(e)$-$1S_{3/2}(h)$ and $1S(e)$-$2S_{3/2}(h)$ transitions) can be well-resolved.

After we get the absorbance of CQD layer without electric field, we need to measure how the photodetector signal is modulated by the applied AC electric field. Using the measurement set-up shown in fig. S8b, we plot the lock-in voltage as a function of wavelength under different electric fields without CQD layer and with CQD layer in fig. S10a and fig. S10b, respectively. We can connect the lock-in voltage with reflectance using following

$$V^E_{without\_\mathrm{C}QDs} = K_1 \times I(\lambda) \times \Delta R(\lambda)_{without\_\mathrm{C}QDs}$$
$$V^E_{with\_\mathrm{C}QDs} = K_2 \times I(\lambda) \times \Delta R(\lambda)_{with\_\mathrm{C}QDs}$$

Here $I(\lambda)$, K_1 and K_2 are the same values as we described previously.

We observe that the device without CQD layer is also sensitive to the applied electric field (fig. S10a), the reason is the permittivity change of any layers in our device or control sample when electric field is applied can make this sensitivity. This is the reason why we need to have the control sample, which is identical to the real device except the CQD layer, to extract the differential transmittance of only CQD layer.

Then, we still use this equation

$$R(\lambda)^{E}_{with\_CQDs} = T(\lambda)^{E}_{CQDs} \times R(\lambda)^{E}_{without\_CQDs}$$

Where, $R(\lambda)^E$ means the reflectance with electric field. Rewriting this equation, we get the following

$$R(\lambda)^{0}_{with\_CQDs} + \Delta R(\lambda)_{with\_CQDs} = [T(\lambda)^{0}_{CQDs} + \Delta T(\lambda)_{CQDs}] \times [R(\lambda)^{0}_{without\_CQDs} + \Delta R(\lambda)_{without\_CQDs}]$$

Expanding this equation and discard the high order term ($\Delta T(\lambda)_{CQDs} * \Delta R(\lambda)_{without\_CQDs}$), we get

$$\Delta T(\lambda)_{CQD} = \frac{\Delta R(\lambda)_{with\_CQDs} - T(\lambda)^{0}_{CQDs} \times \Delta R(\lambda)_{without\_CQDs}}{R(\lambda)^{0}_{without\_CQDs}} = T(\lambda)^{0}_{CQDs} \times \left(\frac{V^{E}_{with\_CQDs}}{V^{chop}_{with\_CQDs}} - \frac{V^{E}_{without\_CQDs}}{V^{chop}_{without\_CQDs}}\right)$$

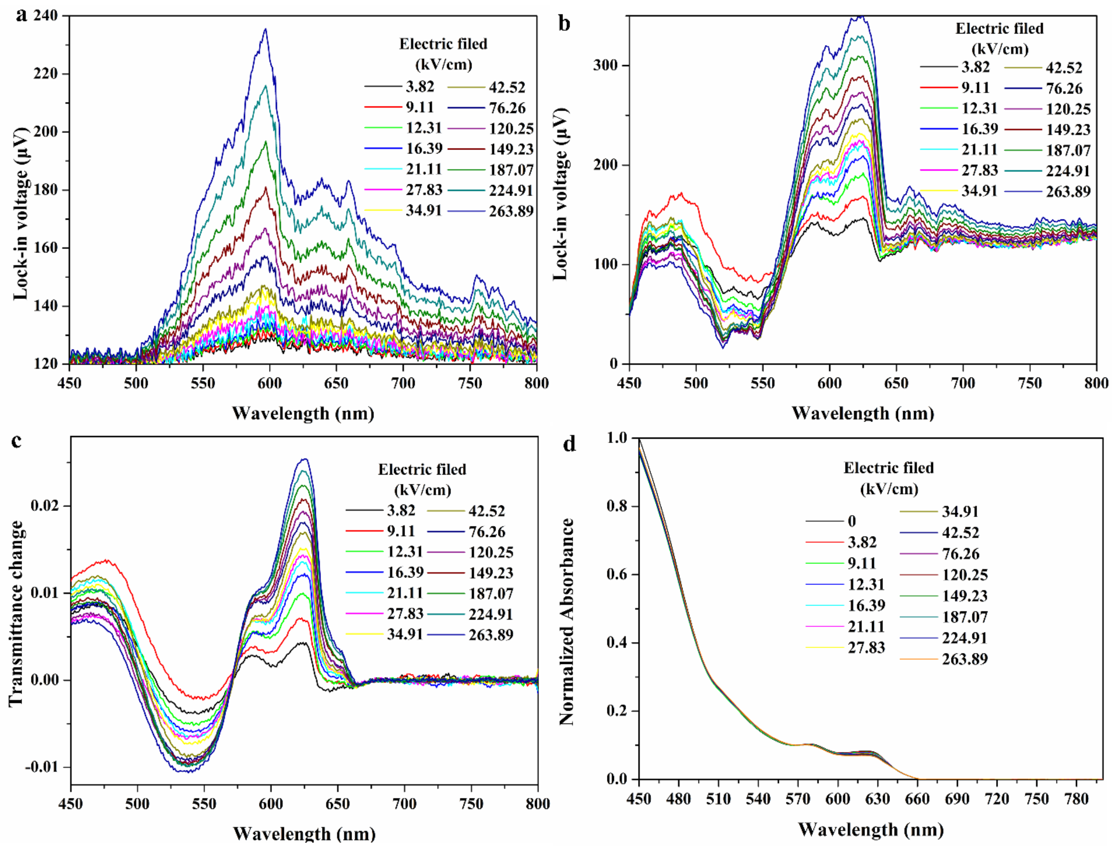

Fig. S10. Steady-state absorbance measurement. (**a**) Lock-in voltages of the device without CQD layer versus electric field. (**b**) Lock-in voltages of the device with CQD layer versus electric field. (**c**) The calculated transmittance change at different electric field. (**d**) Normalized Absorbance converting from the transmittance change at different electric field and the transmittance without electric field.

Note that, a square function modulation is provided by the optical chopper for the first measurement while the AC bias is a sinusoidal function for the second experiment. The lock-in technique measures the sine component at the reference frequency of the signal. According to the Fourier series of the square wave, we just modify the equation with π/4 and calculate the transmittance change (fig. S10c)

$$\Delta T(\lambda)_{CQDs} = T(\lambda)^{0}_{CQDs} \times \frac{4}{\pi} \times \left(\frac{V^{E}_{with\_CQDs}}{V^{chop}_{with\_CQDs}} - \frac{V^{E}_{without\_CQDs}}{V^{chop}_{without\_CQDs}}\right)$$

Finally, we can convert the transmittance to absorbance as shown in fig. S10d (Fig. 3a in main text is the zoom in plot of fig. S10d)

$$A(\lambda)^{E}_{CQD} = -\log_{10}[\Delta T(\lambda)_{CQDs} + T(\lambda)^{0}_{CQDs}]$$

c. Gaussian deconvolution of absorbance data

Each absorbance spectrum is fitted by a sum of four Gaussian curves[20]. As shown in fig. S11, the Gaussian curve for the shortest wavelength (A4, green solid line) is fixed for all absorbance spectra in terms of the magnitude, position and width. We only allow a small floating for the positions of two lowest energy Gaussian curves (A1, navy solid line and A2, blue solid line). The floating range of positions for A1 is from 621.5 nm to 622.5 nm and for A2 is 577 nm to 578 nm. The magnitudes and widths of A1 and A2 are allowed to float during fitting. There is no restriction for the fitting process of A3.

It is important to note that, besides the bleaching of the first and second excitonic transition, electric field will slightly increase the absorbance value at the pump wavelength (532 nm, raw data: 0 kV/cm: 0.1246; 263.89 kV/cm: 0.1262, the increase is ~ 1.3%). This observation is also reported in ref. 20 in which the CdSe CQDs are negatively charged via photo-doping. The reason for this observation is a slight redshift of the absorption spectrum (as we can see easily in PL spectrum at different E-field and also in absorption peak). This absorption redshift is tentatively attributed to the reduced energy required for trion formation in our n-doped CdSe/CdS/ZnS CQDs rather than exciton formation. Thus, this observation could be another evidence to support the electron injection in our device.

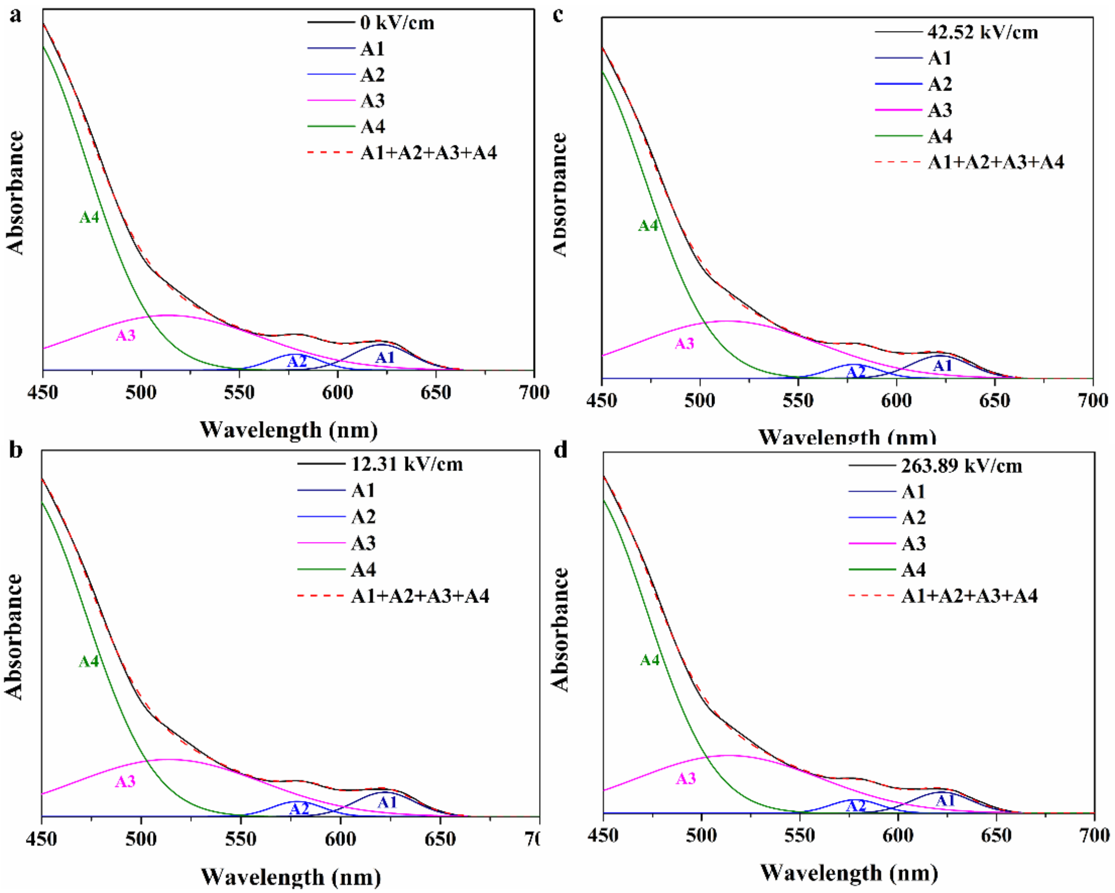

Fig. S11. Gaussian fitting (red dashed line) of absorbance spectra (black solid line). (**a**) Four Gaussian curves to fit absorbance of the CQD layer under zero electric field. (**b-d**) Four Gaussian curves to fit absorbance of the CQD layer in the electric field of 12.31 kV/cm, 42.52 kV/cm, and 263.89 kV/cm, respectively.

According to the above discussion, when the pump fluence (wavelength: 532 nm) is fixed, for larger applied electric field, the absorption cross-section will be slightly larger, and thus, the ASE threshold could be reduced without any change in recombination dynamics. However, absorption cross-section increases by 1.3% at the maximum E field of 263.89 kV/cm; and our threshold reduction of more than 10% was achieved at very low E-field, with which the increase in absorption cross-section is negligible (when E-field is ~21 kV/cm, absorbance is 0.1250, the increase is only ~0.3%).

The integrated area of A3 (fig. S12) remains virtually unchanged with respect to the applied electric field, it implies that no excess electrons in energy states beyond 1S(e) can be induced under the electric field up to ~264 kV/cm.

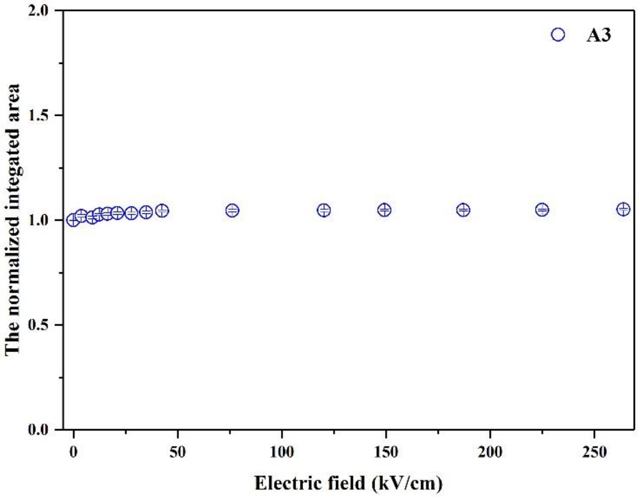

Fig. S12. Integrated area of A3 as a function of electric field.

Section S4. PL dynamics analysis

a. Justification of the lifetime assignment.

In Fig. 4 (the main text), we assign the fast decay component (4.1 ns and 0.75 ns) observed in the trPL data to the singly charged exciton and doubly charged exciton induced by electron injection. To eliminate the possibility that the fast decay is arising from other possibilities (i.e., Auger process or carrier trapping), we have performed fluence dependent lifetime measurement to check the Auger recombination process in our CQDs. Here, we utilized the femtosecond laser as the pump source (100 fs, 400 nm, the picosecond laser does not have enough power to achieve multiple excitons) and streak camera to check the carrier dynamics of the device. We calculate the <N> for each pump fluence. As it can be seen in fig. S13a, when the fluence is low (exciton per quantum dot: <N> is smaller than 0.1), the PL decay can be fitted by a mono-exponential decay function with a lifetime of ~20 ns. As the fluence is furtherly increased, we start to observe the build-up of a faster decay component, which is attributed to the decay of the multiexciton where the non-radiative Auger recombination can be resolved[27]. Specifically, when the fluence is 50 μJ/cm^2 (<N> ~1.21), 34% of the CQDs have multiple-excitons corresponding to the Poison distribution, the lifetime of the fast decay component is 600±11 ps. This fast decay is quite different from the fast decay component (~ 750 ps) observed in our device when electric field is applied. This could be the evidence that the fast decay in our device with electric field is not caused by Auger process. It is worth to note that we cannot increase the fluence further since the ASE threshold is ~53 μJ/cm^2, after which the decay process is dominated by ASE. Then, we can calculate the Auger lifetime using the following equation[7,43]

$$\tau_{AR}{}^{-1} = \tau_{XX}{}^{-1} - 4\tau_{X}{}^{-1}$$

Where $4\tau_X{}^{-1}$ is the radiative recombination rate of the biexciton, and the factor 4 indicates the number of recombination channel of the biexciton. The extracted Auger lifetime of biexciton in our CQDs is 730 ± 47 ps, which is agreeable with the biexciton Auger lifetime (~750 ps) of CdSe/CdS/ZnS CQDs in ref. 35 and slightly faster than the Auger lifetime (~1.25 ns) of CdSe/CdS reported in Ref. 43. Furthermore, the slower lifetime component, corresponding to the radiative decay, is also slightly accelerated (~18.9 ns) compared to the case at low pump fluence due to the multiple exciton radiative enhancement[31].

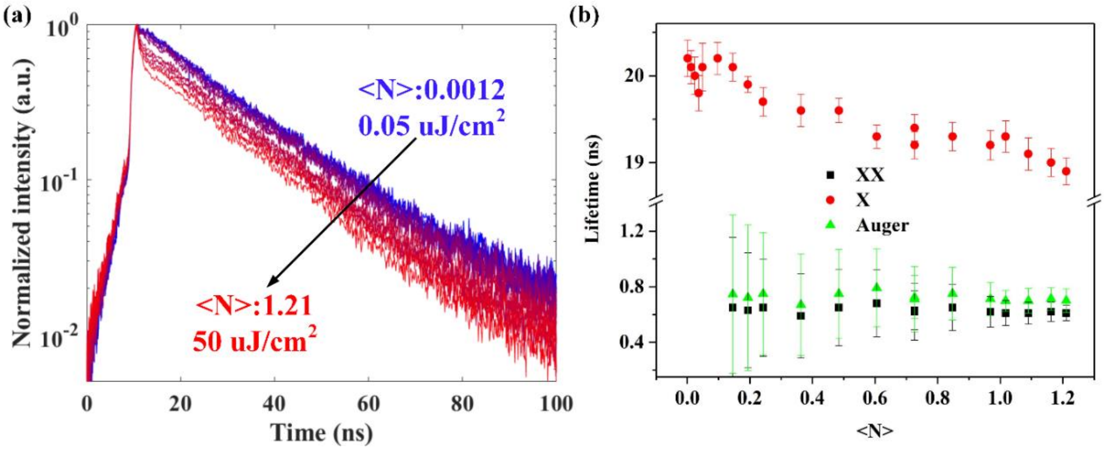

Fig. S13. Fluence-dependent lifetime probe at peak wavelength. (**a**) The decay traces. (**b**) Fitting result.

Another possibility which can change the decay trace is the trapping process, as claimed in a blinking study[34]. This process can also be ignored in our QDs because the trPL data can be fitted by a mono-exponential decay when the pump fluence is low. This means the active trap states are not observed[31]. Moreover, the recombination of trapped carriers is a rather slow process which will give us a delay emission (> 100 ns), as reported in Ref. 44, however, our lifetime decay did not show this slow component. The negligible active trap density is also consistent with the high quantum yield in CQDs.

Now, turning back to our electric field dependent trPL measurement data presented in Fig. 4. The first thing we can conclude is that the lifetime changing is caused by only the applied electric field. Then, we should notice that, with increasing electric field, other two discrete fast components appear (4.1 ns and 0.75 ns), these three decay channels are quite different from one other. Moreover, the electric field changes only the amplitude ratio among these three components. This suggests that the long-time decay originates from radiative recombination of neutral QDs, the other two faster components of the trPL are from new generated groups. The electric field only changes the population distribution not the decay process.

The two fast components (4.1 ns and 0.75 ns) in our device with E-field and low fluence (N < 0.1) are also distinguished from the fast decay component (biexciton decay: ~ 600 ps) when pumping at high fluence (N > 1.2) and without E-field. With fixed low excitation level when we conducted the measurement for our device with E-field, Auger process is negligible. Therefore, we can safely conclude that the new fast decay components are arising from the charged quantum dots. A similar discussion can also be found in ref. [1,7,21,25].

b. Determine the radiative enhancement factor in singly and doubly charged CQDs

When a CQD is charging, the extra electrons occupy the conduction band, the radiative recombination will be enhanced. We can deduce the radiative lifetime of singly charged CQDs and doubly charged CQDs using this relationship

$$t_{radiative} = \frac{20.1}{\alpha}$$

Where 20.1 ns is the radiative lifetime of neutral exciton and α is the radiative enhancement factor. Statistically, α is 2 for singly and doubly charged exciton. However, recent reports[34] show that electron repulsion effect occurred in charged CQDs results in a factor less than 2. To determine α in charged CQDs, we rescale the intensity of PL decay curves so that they all match to each other at the long-time tail (20 ns ~ 60 ns) which is the decay feature of the neutral CQDs only. The difference between decay curve of CQDs in electric field and that of CQDs in no electric field is associated to charged CQDs. We fit the PL dynamics using the model proposed in ref. 7. The subtracted PL dynamics can be expressed as below with consideration of a Poisson distribution for the number of neutral exciton, singly charged exciton and doubly charged exciton.

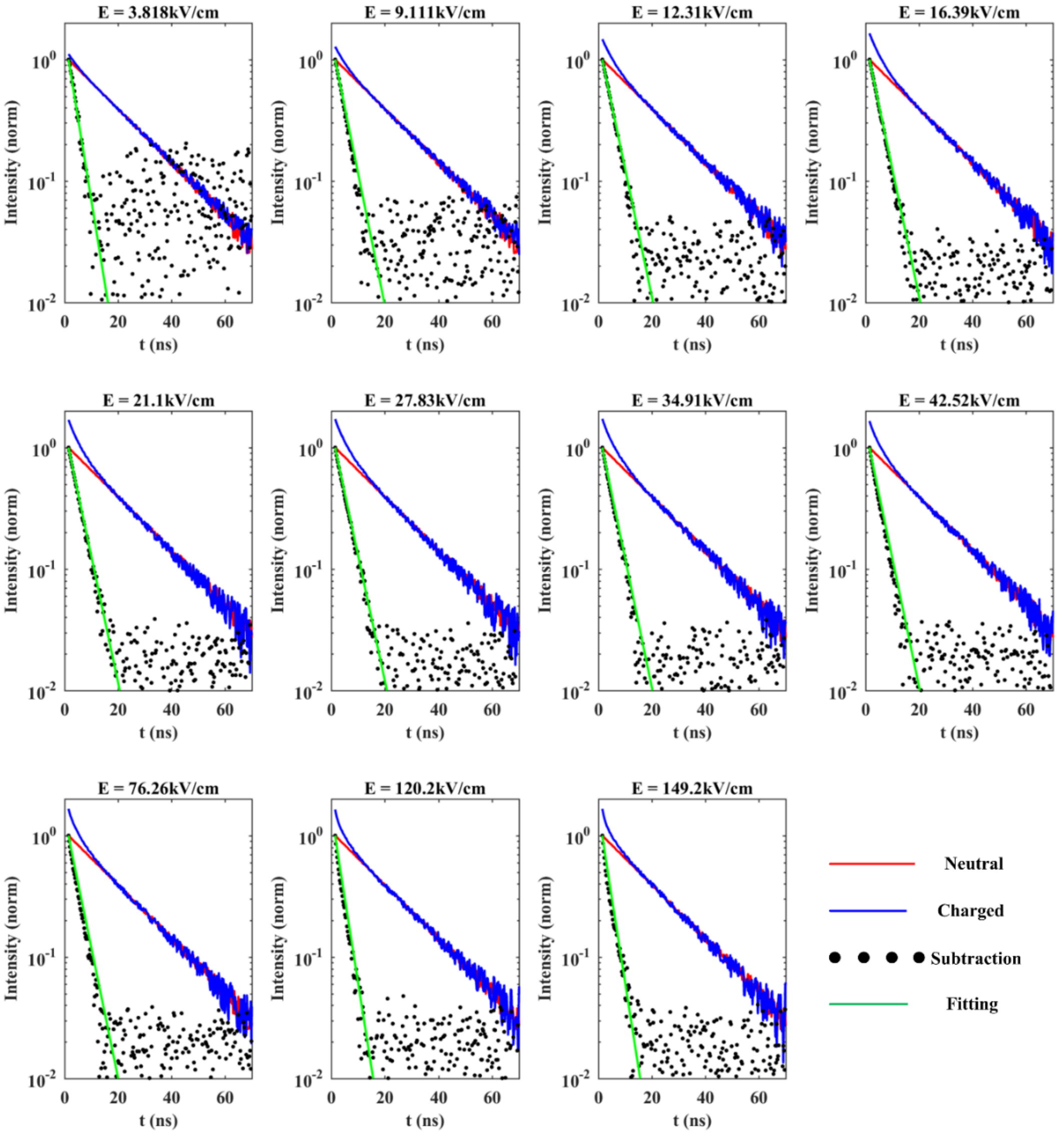

Fig. S14. Fitting results of the subtraction of PL dynamics at different electric fields. The red solid line is the PL dynamics of neutral CQD layer. The blue solid line is the PL dynamics of CQD layer at different electric field. The curves are scaled by a ratio to match the PL decay curve of neutral CQD layer in long time range (20 ns ~ 60 ns). The black dot is the normalized subtraction of the blue line and red line. The green solid line is the fitting results using the described model.

$$PL\_decay_{subtracted} = \frac{\sum_{k=1}^{\infty} P(\mathrm{k}) \times \alpha \times e^{-\frac{t}{\tau_k}}}{A_{<n_e>} \times P(0)}$$

$$P(\mathrm{k}) = \frac{< n_e >^k \times e^{-k}}{k!}$$

Where $A_{<n_e>}$ is the scaled constant for PL decay of CQD layer when the average electron per dot is n_e, P(k) is the Poisson probability when the electron number in the CQD is k, τ_k is the recombination lifetime and α is the radiative enhancement factor, respectively. Given that $<n_e>$ in our case is less than 1 (maximum is about 0.4), we can ignore the contributions of those k >= 3 components. And then plug in our measured $<n_e>$, lifetime and we got the radiative enhancement factor α = 1.517, to show very good fitting results of the subtracted PL decays, as shown in fig. S14.

Section S5. Kinetics model

a. Rate equations

Here, we modify the kinetic model proposed in ref. 7 and calculate the stimulated emission process in mix population of neutral and charged CQDs. fig. S15 shows the transition processes which are responsible for stimulated emission. In neutral CQDs, we need biexciton to achieve the population inversion. For singly charged CQDs, the transitions involved in stimulated emission are only between $|X^{1-}>$ and |GS>. For doubly charged CQDs, due to the optical transparency, the transition involved in optical gain calculates are only $|X^{2-}>$ to |GS> stimulated emission. All the multiple-exciton states in singly or doubly charged CQDs will non-radiatively recombine very fast and we consider them having no contribution to the process.

We now consider the CQDs in our device under different electric field which is converted to charged CQD population in our model. Besides those transitions involved in the stimulated emission, we take the waveguide photon losses, decay of exciton/biexciton and pumping laser into consideration and get the following rate equations:

$$\frac{dP_{GS,0}}{dt}=\frac{P_{\mathrm{ex},0}P_{ph}}{\tau_{sti}}+\frac{P_{\mathrm{ex},0}}{\tau_{\mathrm{ex},0}}-\frac{4P_{GS,0}P_{ph}}{\tau_{sti}}-P_{GS,0}R_{pump}$$

$$\frac{dP_{GS,1}}{dt}=\frac{2P_{ex,1}P_{ph}}{\tau_{sti}}+\frac{P_{ex,1}}{\tau_{ex,1}}-\frac{2P_{GS,1}P_{ph}}{\tau_{sti}}-P_{GS,1}R_{pump}$$

$$\frac{dP_{GS,2}}{dt}=\frac{2P_{ex,2}P_{ph}}{\tau_{sti}}+\frac{P_{ex,2}}{\tau_{ex,2}}-P_{GS,2}R_{pump}$$

$$\frac{dP_{\mathrm{ex},0}}{dt}=\frac{P_{\mathrm{biex},0}}{\tau_{\mathrm{biex},0}}-\frac{P_{\mathrm{ex},0}}{\tau_{\mathrm{ex},0}}+\frac{4P_{GS,0}P_{ph}}{\tau_{sti}}-\frac{P_{\mathrm{ex},0}P_{ph}}{\tau_{sti}}+\frac{4P_{\mathrm{biex},0}P_{ph}}{\tau_{sti}}+P_{GS,0}R_{pump}-P_{\mathrm{ex},0}R_{pump}$$

$$\frac{dP_{ex,1}}{dt}=-\frac{P_{ex,1}}{\tau_{ex,1}}+\frac{2P_{GS,1}P_{ph}}{\tau_{sti}}-\frac{2P_{ex,1}P_{ph}}{\tau_{sti}}+P_{GS,1}R_{pump}$$

$$\frac{dP_{ex,2}}{dt}=-\frac{P_{ex,2}}{\tau_{ex,2}}-\frac{2P_{ex,2}P_{ph}}{\tau_{sti}}+P_{GS,2}R_{pump}$$

$$\frac{dP_{\mathrm{biex},0}}{dt}=-\frac{P_{\mathrm{biex},0}}{\tau_{\mathrm{biex},0}}+\frac{P_{\mathrm{ex},0}P_{ph}}{\tau_{sti}}-\frac{4P_{\mathrm{biex},0}P_{ph}}{\tau_{sti}}+P_{\mathrm{ex},0}R_{pump}$$

$$\frac{dP_{ph}}{dt}=-\frac{P_{ph}}{\tau_c}+\frac{4P_{\mathrm{biex},0}P_{ph}}{\tau_{sti}}-\frac{4P_{GS,0}P_{ph}}{\tau_{sti}}+\frac{P_{\mathrm{ex},0}\gamma}{\tau_{\mathrm{ex},0}}+\frac{P_{\mathrm{biex},0}\gamma}{\tau_{\mathrm{biex},r,0}}+\frac{2P_{ex,1}P_{ph}}{\tau_{sti}}-\frac{2P_{GS,1}P_{ph}}{\tau_{sti}}+\frac{P_{ex,1}\gamma}{\tau_{ex,\mathrm{r},1}}+\frac{2P_{ex,2}P_{ph}}{\tau_{sti}}+\frac{P_{ex,2}\gamma}{\tau_{ex,r,2}}$$

Where P_{ph} is the photon density, τ_{sti} is the lifetime of stimulated absorption/emission, $\mathrm{R}_{\mathrm{pump}}$ is the exciton pumping rate (proportional to the laser pump intensity), τ_c is the lifetime of cavity photons which represents all the potential losses for waveguide-coupling photons in our model. $P_{GS,0}$, $P_{GS,1}$ and $P_{GS,2}$ are the unexcited population fraction of neutral, singly and doubly charged CQDs, respectively. $P_{\mathrm{ex},0}$, $P_{\mathrm{ex},1}$ and $P_{\mathrm{ex},2}$ are the exciton population fraction of neutral, singly and doubly charged CQDs, respectively. $P_{\mathrm{biex},0}$ is the biexciton population fraction of neutral CQDs. $\tau_{\mathrm{ex},0}$, $\tau_{ex,1}$ and $\tau_{ex,2}$ are the exciton lifetime of neutral, singly and doubly charged CQDs, respectively. $\tau_{ex,\mathrm{r},1}$ and $\tau_{ex,r,2}$ are the radiative lifetime of biexciton in singly charged and doubly charged CQDs, respectively. $\tau_{\mathrm{biex},0}$ are the biexciton lifetime in neutral CQDs and $\tau_{biex,r}$ is the radiative lifetime of biexciton in neutral CQDs.

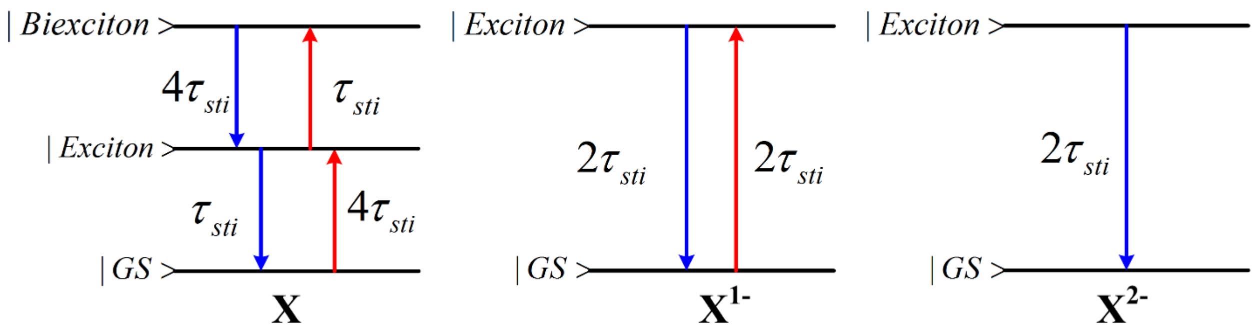

Fig. S15. Optical transition processes in neutral CQDs (*X*), singly charged CQDs (X^{1-}), and doubly charged CQDs (X^{2-}). |GS> means the ground state.

Considering the direction of spontaneous emission is random and not all the spontaneous emission photons can contribute to the stimulated emission, γ is the coupling efficiency defined as the fraction of spontaneous emission photons which are coupled into the waveguide. COMSOL simulation is performed to determine the coupling efficiency, as shown in fig. S16. Basically, we put the dipole oscillating in Y direction (In-plane dipole, fig. S16a) and Z direction (Out-plane dipole, fig. S16b) inside the capacitor structure, and monitor the energy propagated along the Y direction (edge emission). A coupling efficiency of ~2% is obtained for In-plane dipole and ~10% for Out-plane dipole as shown in the electric field distribution fig. S16b. According to R. Scott's works[45], the population fraction in CdSe CQDs of In-plane dipole is 68% while for Out-plane dipole is 32%. Hence, we adopt the coupling efficiency of ~4.5% in our calculation.

All these three groups of rate equations are based on the following assumptions:

(1) The exciton pumping rate are the same for all three cases. This is reasonable because the excitation photon is at high energy compared to band gap, so the absorption is not affected by charges in the CQDs which are at the band edge.

(2) We do not consider the interaction among CQDs.

(3) We do not consider the contributions from multiple excitons (≥3 for neutral CQD and ≥2 for charged CQDs) as they do not directly contribute to stimulated emission at the band edge and the enhanced Auger process will make them non-radiatively recombined significantly fast.

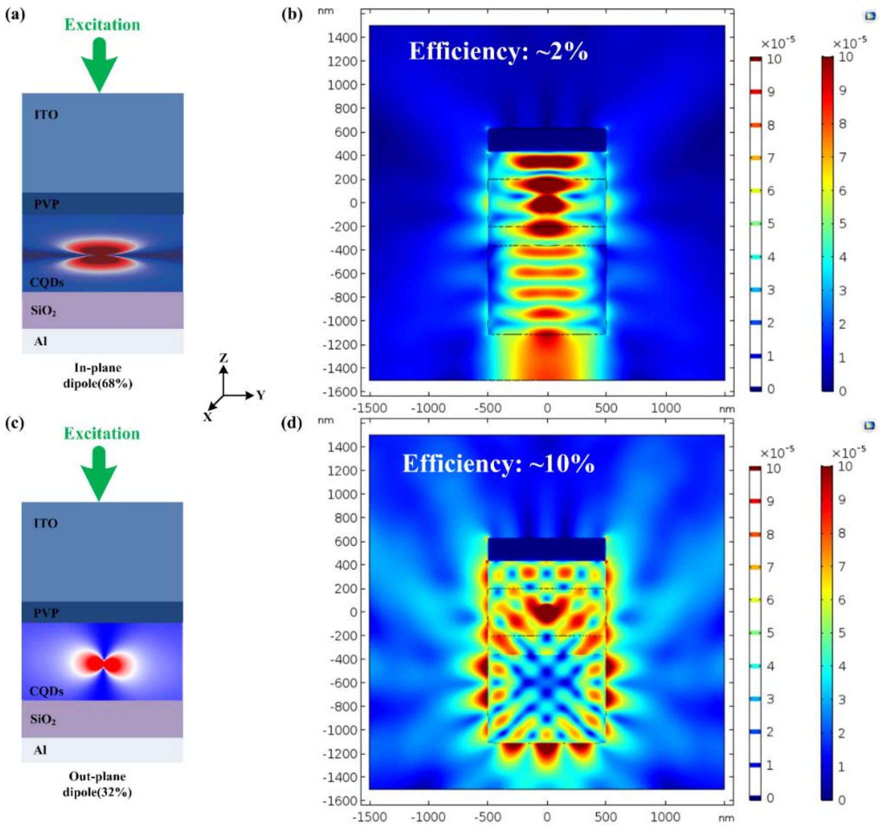

Fig. S16. COMSOL simulation to determine the coupling efficiency. (**a**) The In-plane dipole inside the capacitor structure. (**b**) Calculated electric field distribution of the In-plane dipole. (**c**) The Out-plane dipole inside the capacitor structure. (**d**) Calculated electric field distribution of the Out-plane dipole.

b. Initial conditions

Below we list the initial conditions used for calculation:

(1) when t = 0, the value of $P_{GS,0}$, $P_{GS,1}$ and $P_{GS,2}$ under different electric field used in the rate equation is from the PL dynamics analysis (main text, Fig. 4). And $P_{GS,0} + P_{GS,1} + P_{GS,2} = 1$.

At t = 0, the population fraction of exciton ($P_{\mathrm{ex},0}$, $P_{\mathrm{ex},1}$ and $P_{\mathrm{ex},2}$), biexciton ($P_{\mathrm{biex},0}$) and cavity photon (P_{ph}) are all zero.

(2) R_{pump} = abs_cs * Pump_fluence * Laser_pulse_shape. Here, abs_cs means absorption cross section of CQDs. We should choose the abs_cs value which make the simulated threshold be consistent with 891.48 μJ/cm2 (experimental result) for neutral CQDs. Laser_pulse_shape is Gaussian pulsed with 500 ps FWHM of our laser.

(3) τ_{sti} of 10 ps is cited the number in ref 6 and ref 7.

(4) τ_c of 13.3 ps is estimated which corresponds to a photon propagates 4 mm (our strip length) along the waveguide.

(5) Other lifetime data used here is from experimental results of PL dynamics (main text, Fig. 4).

c. Simulated population dynamics

After we plug the initial conditions into the modified rate equations, the population dynamics of ground state exciton, biexciton and cavity photon can be obtained. fig. S17 presents the photon emission density as a function of pumping intensity to show the transition from spontaneous emission to ASE at some electric field. fig. S18 presents the 2d emitted photon decay map under each electric field at the pump fluence of 800 μJ/cm^2 and 1000 μJ/cm^2, respectively. This is similar to Fig. 5b and 5c in the main text without normalization to show only the strong intensity of light when ASE happens. In addition, two examples when the applied electric field is 21 kV/cm are presented to show the simulated dynamics (below the threshold: 100 μJ/cm^2, fig. S19; above the threshold: 1000 μJ/cm^2, fig. S20);

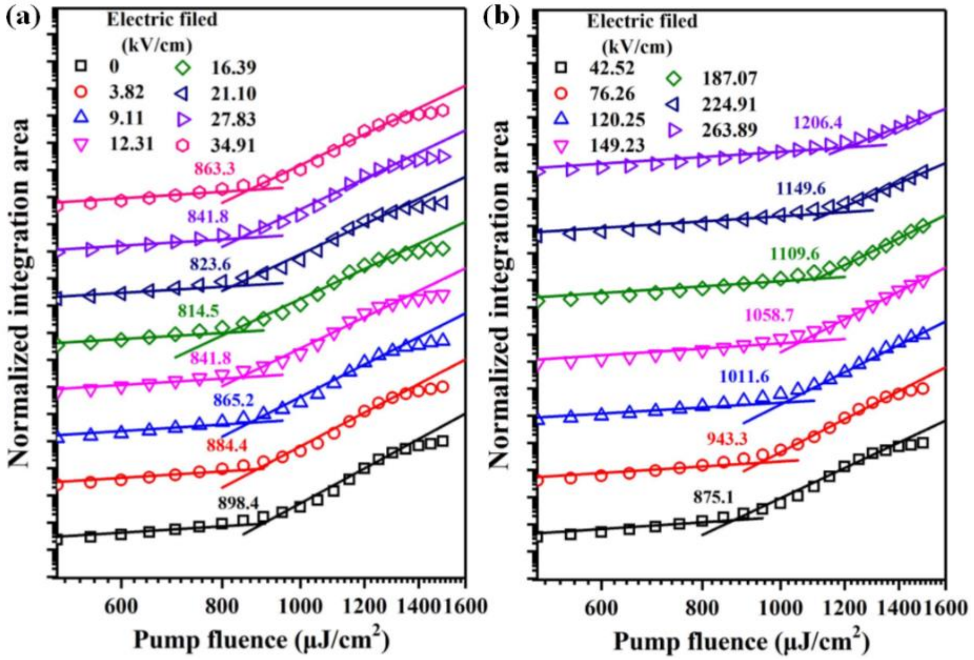

Fig. S17. Photon emission density as a function of pumping intensity.

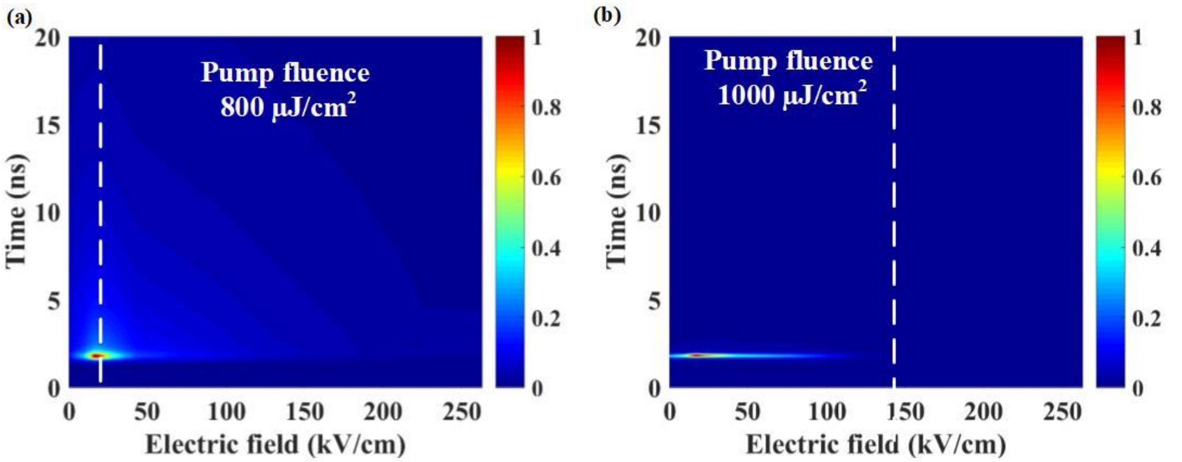

Fig. S18. The 2d emitted photon decay map under each electric field at the pump fluence of 800 μJ/cm^2 (a) and 1000 μJ/cm^2 (b). At 800 μJ/cm^2, the white dash line locates at the e-field threshold. At 1000 μJ/cm^2, the ASE can be observed under the electric field smaller than 149.2 kV/cm (white dash line).

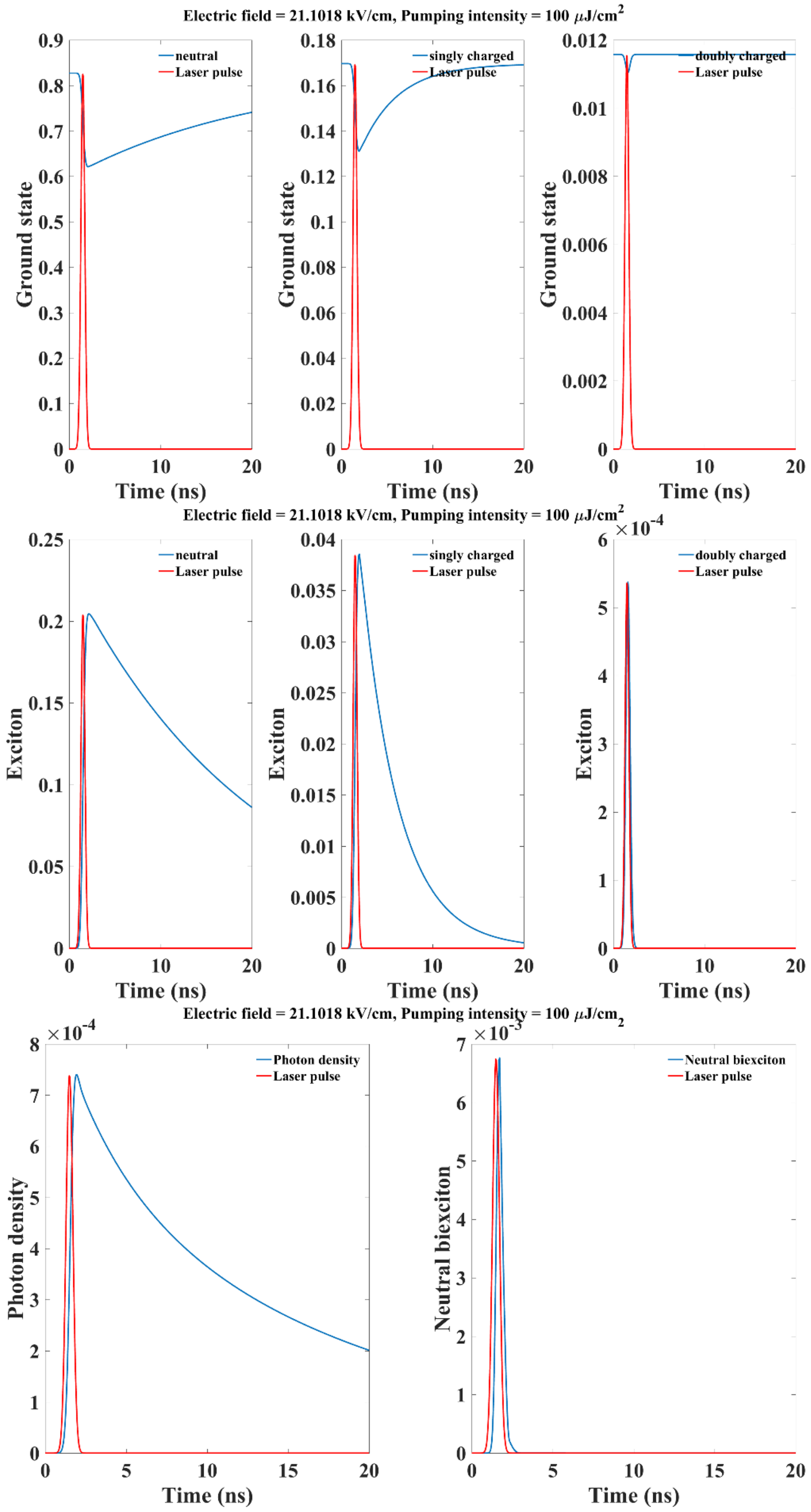

Fig. S19. Population dynamics under an electric field of ~21 kV/cm and with a pump fluence of 100 μJ/cm^2. Red solid line is the normalized laser pulse as a function of time. Blue solid line is the population dynamics.

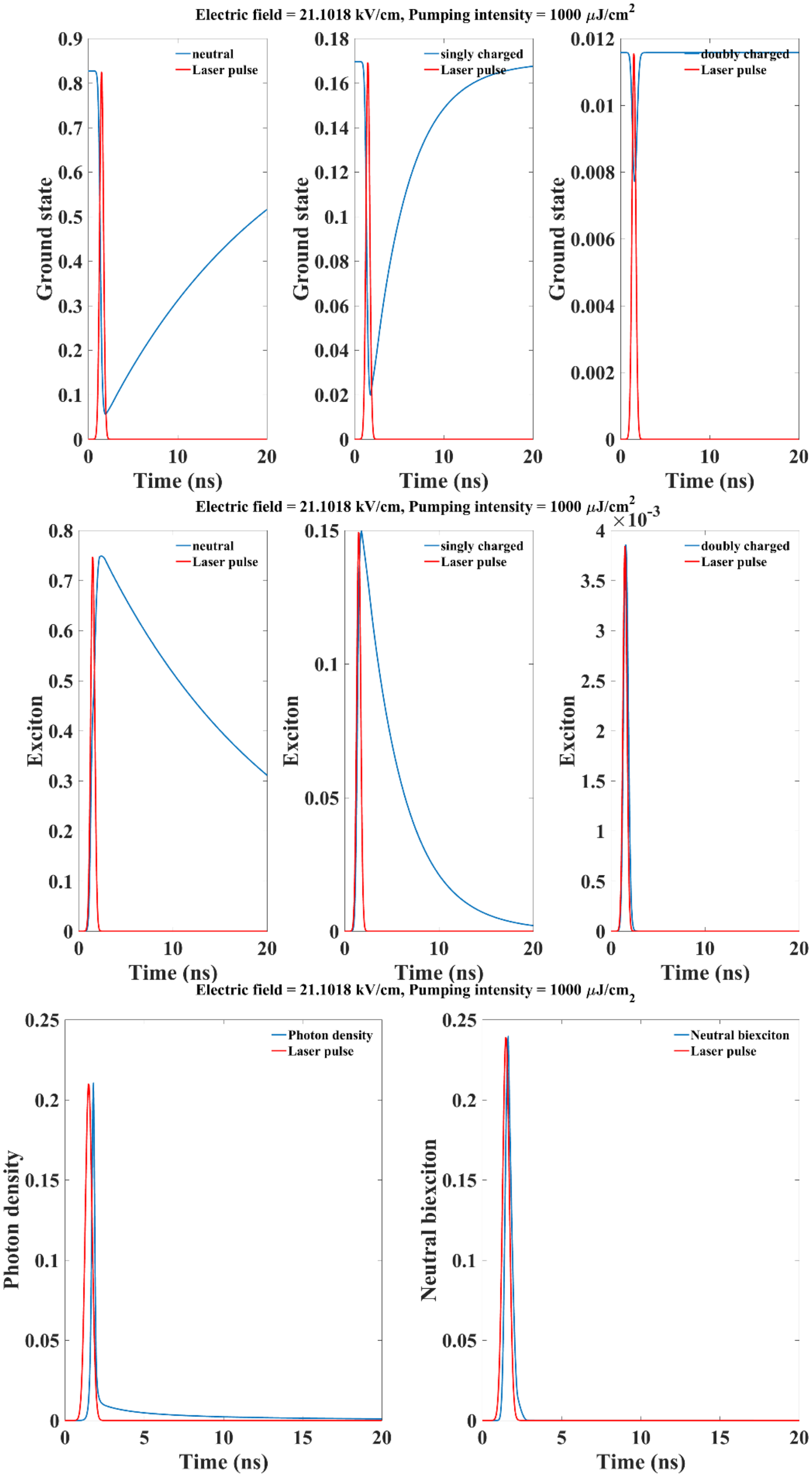

Fig. S20. Population dynamics under an electric field of ~21 kV/cm and with a pump fluence of 1000 μJ/cm^2. Red solid line is the normalized laser pulse as a function of time. Blue solid line is the population dynamics.